Hybrid Dion–Jacobson 2D Lead Iodide Perovskites — **Source link** ⧉

Lingling Mao, Weijun Ke, Laurent Pedesseau, Yilei Wu ...+7 more authors

Institutions: Northwestern University, University of Rennes, Argonne National Laboratory

Related papers:

- High-efficiency two-dimensional Ruddlesden–Popper perovskite solar cells

- Ruddlesden-Popper Hybrid Lead Iodide Perovskite 2D Homologous Semiconductors

- 2D Homologous Perovskites as Light-Absorbing Materials for Solar Cell Applications

- A Layered Hybrid Perovskite Solar-Cell Absorber with Enhanced Moisture Stability

- Organometal Halide Perovskites as Visible-Light Sensitizers for Photovoltaic Cells

Share this paper: 𝐟 🐦 in ✉

View more about this paper here: https://typeset.io/papers/hybrid-dion-jacobson-2d-lead-iodide-perovskites-25gjwpahur

Hybrid Dion-Jacobson 2D Lead Iodide Perovskites

Lingling Mao, Weijun Ke, Laurent Pedesseau, Yilei Wu, Claudine Katan, Jacky Even, Michael Wasielewski, Constantinos Stoumpos, Mercouri Kanatzidis

HAL Id: hal-01714840
https://hal.archives-ouvertes.fr/hal-01714840

Hybrid Dion-Jacobson 2D Lead Iodide Perovskites

Lingling Mao[1], Weijun Ke[1], Laurent Pedesseau[3], Yilei Wu[1], Claudine Katan[4], Jacky Even[3], Michael R. Wasielewski[1,2], Constantinos C. Stoumpos*[1] and Mercouri G. Kanatzidis*[1,2]

[1] Department of Chemistry and [2] Argonne-Northwestern Solar Energy Research (ANSER) Center, Northwestern University, Evanston, Illinois 60208, United States

[3] Univ Rennes, INSA Rennes, CNRS, Institut FOTON – UMR 6082, F-35000, Rennes, France

[4] Univ Rennes, ENSCR, INSA Rennes, CNRS, ISCR (Institut des Sciences Chimiques de Rennes) – UMR 6226, F-35000 Rennes, France

ABSTRACT: The three-dimensional hybrid organic-inorganic perovskites have shown huge potential for use in solar cells and other optoelectronic devices. Although these materials are under intense investigation, derivative materials with lower dimensionality are emerging offering higher tunability of physical properties and new capabilities. Here we present two new series of hybrid two-dimensional (2D) perovskites that adopt the Dion-Jacobson (DJ) structure-type, which are the first complete homologous series reported in halide perovskite chemistry. Lead iodide DJ perovskites adopt a general formula $A'A_{n-1}Pb_nI_{3n+1}$ (A' = 3-(aminomethyl)piperidinium (3AMP) or 4-(aminomethyl)piperidinium (4AMP), A = methylammonium (MA)). These materials have layered structures where the stacking of inorganic layers is unique as they lay exactly on top of another. With a slightly different position of the functional group in the templating cation 3AMP and 4AMP, the as-formed DJ perovskites show different optical properties, with the 3AMP series having smaller band gaps than the 4AMP series. Analysis on the crystal structures and Density functional theory (DFT) calculations suggest that the origin of the systematic band gap shift is the strong but indirect influence of the organic cation on the inorganic framework. Fabrication of photovoltaic devices utilizing these materials as light absorbers reveal that $(3AMP)(MA)_3Pb_4I_{13}$ has the best power conversion efficiency (PCE) of 7.32%, which is much higher than corresponding $(4AMP)(MA)_3Pb_4I_{13}$.

Introduction

Hybrid organic-inorganic halide perovskites materials with three-dimensional (3D) AMX_3 structures enable solar cells with power conversion efficiency (PCE) over 22%.[1-7] With impressive structural diversity and great potential in optoelectronic applications, two-dimensional (2D) hybrid organic-inorganic halide perovskites are evolving into an important class of high-performance semiconductors.[8-22] 2D halide perovskites, $A'_2A_{n-1}M_nX_{3n+1}$ or $A'A_{n-1}M_nX_{3n+1}$, (A' = 1+ or 2+, A = 1+ cation, M = Pb^{2+}, Sn^{2+}, Ge^{2+}, Cu^{2+}, Cd^{2+} etc., X = Cl^-, Br^- and I^-), are classified depending on the stacking orientation of the inorganic layers ((100), (110) or (111) with respect to the ideal cubic perovskite), but also on the number of the inorganic layers (n = 1, 2, 3 etc, in the chemical formula).[10, 23] The single-layered 2D perovskites (n = 1) which have a general formula of A_2MX_4 or AMX_4 (have been extensively explored and there is a large number of structural types reported to date, differing in the nature of the organic spacers and the configuration of the inorganic layers.[10, 24-25] For the higher number of layers (n ≥ 2), however, there are only few crystallographically characterized examples: $(PEA)_2(MA)_{n-1}Pb_nI_{3n+1}$ (n = 2, 3)[14, 26] (PEA = phenylethylammonium, MA = methylammonium), $(BA)_2(MA)_{n-1}Pb_nI_{3n+1}$ (n = 2 - 5) (BA = butylammonium),[27-28] $(GA)(MA)_nPb_nI_{3n+1}$ (GA = guanidinium, n = 2 - 3),[29] $(BA)_2(MA)_{n-1}Sn_nI_{3n+1}$ (n = 2 - 3),[23, 30] $(CH_3C_6H_4CH_2NH_3)_2(MA)Pb_2I_7$,[31] $(HO_2C(CH_2)_3NH_3)_2(MA)Pb_2I_7$,[32] $(C_4H_3SCH_2NH_3)_2(MA)Pb_2I_7$,[33] $(EA)_4Pb_3X_{10}$[34] (X = Cl, Br) (EA = ethylammonium), $(BA)_2(MA)_2Pb_3Br_{10}$[35] and

$Cs_2[C(NH_2)_3]Pb_2Br_7$.[36] The layered structures, historically, can be divided into several categories, based on the nomenclature of oxide perovskites:[37] a) Ruddlesden-Popper (RP) phases,[27, 38] b) Dion-Jacobson (DJ)[39-40] (Figure 1a), the oxide perovskite specific c) Aurivilius (AV) phases[41] and the halide perovskite specific d) alternating cation in the interlayer space (ACI) type.[29] The differences between these categories are shown in the relative stacking of the layers. The halide perovskites are dominated by the RP archetypes which are characterized by two offset layers per unit cell (Figure 1a). having pairs of interdigitated interlayer spacers (1+). The DJ perovskites feature divalent (2+) interlayer spacers, requiring only one cation per formula unit,[42-45] and tend to adopt the $RbAlF_4$ structure-type.[46] Because of this, DJ perovskites have a rich configurational stereochemistry with the layers being able to stack in a perfect (0,0 displacement, as reported here) or imperfect (0, ½ or ½, ½ displacements) arrangement according to the steric demands of the interlayer cations, as derived from oxide chemistry.[47] The oxide DJ perovskites have been studied extensively due to their interesting ion-exchange[48-49] and intercalation[50] properties. In halide perovskites, beyond the single-layer perovskites (n = 1) very little is known regarding the higher n-members in the perovskite hierarchy.
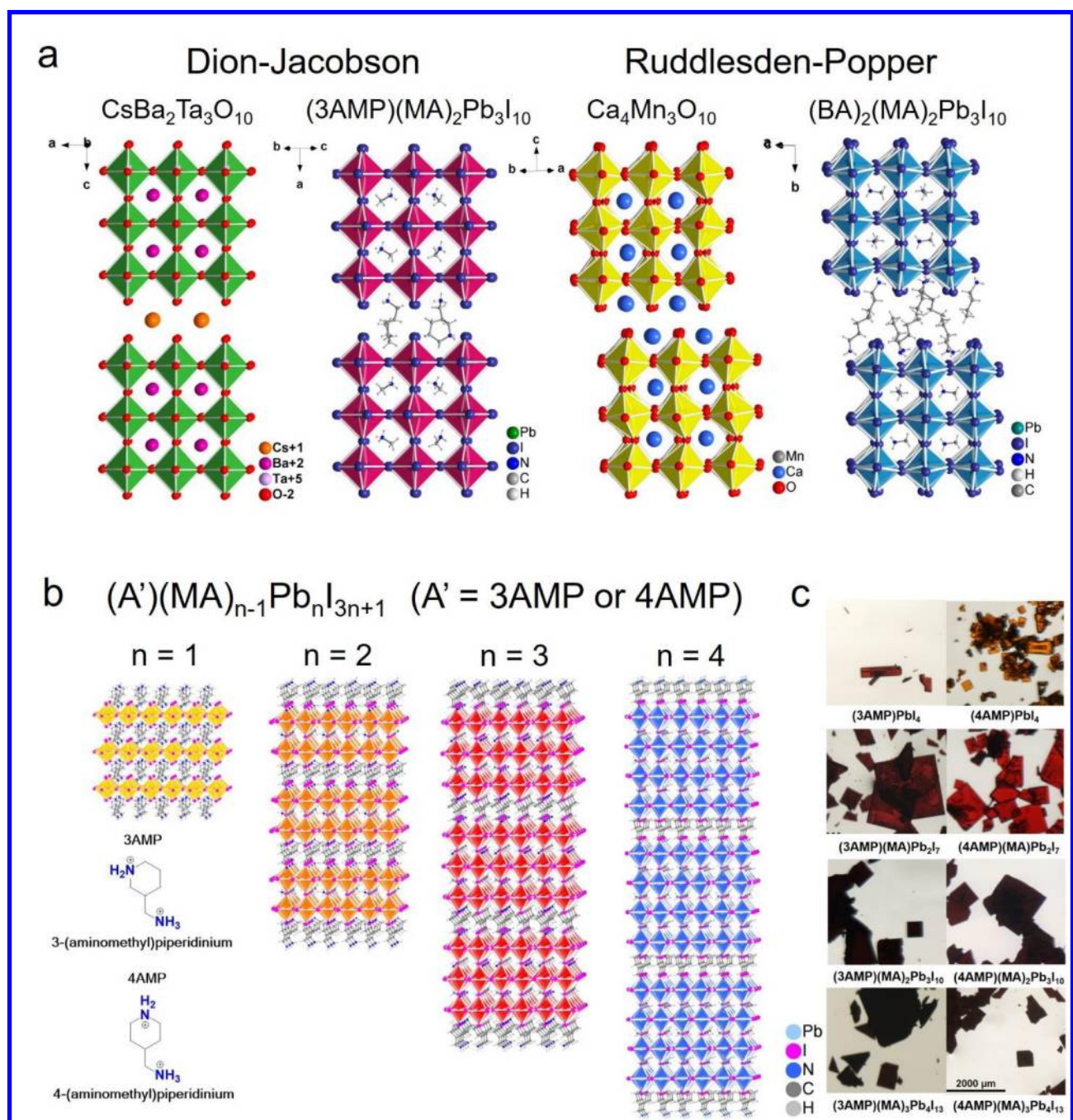
Figure 1. a, Comparison between Dion-Jacobson phases and Ruddlesden-Popper phases for both oxide and halide perovskite. Crystal structure of $CsBa_2Ta_3O_{10}$, $Ca_4Mn_3O_{10}$ and $(BA)_2(MA)_2Pb_3I_{10}$ are adopted from reference 41, 38 and 27. **b,** General crystal structure of the two series of DJ perovskite reported here, from n = 1 to 4. Structures of the cation 3AMP and 4AMP are listed in the lower left corner. **c,** Optical images of the 3AMP and 4AMP crystals. Scale bar on the bottom right applies to all.

Here we report the first examples of hybrid DJ hybrid 2D lead iodide perovskites which consist of thick perovskite slabs (n>1) with layer number (n) ranging from 1 to 4. We describe two new DJ perovskite series based on bivalent (+2) organic cations deriving from a piperidinium (C_5NH_{12}) organic backbone (Figure 1b). The new DJ perovskites are built from 3AMP (3AMP = 3-(aminomethyl)piperidinium) and 4AMP (4AMP = 4-(aminomethyl)piperidinium) cations between the layers ("spacers") and methylammonium (MA) cations inside the 2D layers ("perovskitizers") to form (A') $(MA)_{n-1}Pb_nI_{3n+1}$ (A' = 3AMP or 4AMP, n = 1-4) homologous series.[51] With the exception of the n = 1 members, the 3AMP and 4AMP series with a

representative crystal structure sequence shown in Figure 1b. We find that the difference in the position of the -$CH_2NH_3^+$ group on the piperidine chair (3- and 4- position with respect to the piperidine nitrogen) influence the crystal structure through different hydrogen bonding modes, which is further reflected on the distortion of the inorganic layers. This difference has a major impact on the optical and electronic properties, which see a narrowing of the bandgap and an enhanced charge transport performance for the least distorted structure (3AMP). Density functional theory calculations (DFT)

Table. 1 Crystal data and structure refinement for A′MA$_{n-1}$Pb$_n$I$_{3n+1}$ (A' = 3AMP or 4AMP).

Compound	(3AMP)PbI$_4$	(3AMP) (MA)Pb$_2$I$_7$	(3AMP) (MA)$_2$Pb$_3$I$_{10}$	(3AMP) (MA)$_3$Pb$_4$I$_{13}$
Empirical formula	C$_6$N$_2$H$_{16}$PbI$_4$	(C$_6$N$_2$H$_{16}$)(CH$_3$NH$_3$)Pb$_2$I$_7$	(C$_6$N$_2$H$_{16}$)(CH$_3$NH$_3$)$_2$Pb$_3$I$_{10}$	(C$_6$N$_2$H$_{16}$)(CH$_3$NH$_3$)$_3$Pb$_4$I$_{13}$
Crystal system	Monoclinic			
Space group	*P2$_1$/c*	*Ia*	*Pa*	*Ia*
Unit cell dimensions	a = 8.6732(6) Å, b = 18.4268(9) Å, c = 20.4522(14) Å, β = 99.306(6) °	a = 8.8581(11) Å, b = 8.8607(4) Å, c = 33.4749(5) Å, β = 90°	a = 8.8616(3) Å, b = 8.8624(3) Å, c = 23.0316(7) Å, β = 90°	a = 8.8627(18) Å, b = 8.8689(18) Å, c = 58.842(12) Å, β = 90°
Volume (Å^3)	3225.67(35)	2627.4(3)	1808.79(10)	4625.1(16)
Z	8	4	2	4
Density (g/cm^3)	3.4224	3.6681	3.8024	3.8645
Indepd. refl.	5033 [R$_{int}$ = 0.1102]	4422 [R$_{int}$ = 0.0202]	8035 [R$_{int}$ = 0.0361]	5893 [R$_{int}$ = 0.0405]
Data / restraints / param.	5033 / 32 / 145	4422 / 17 / 115	8035 / 28 / 163	5893 / 19 / 201
Final R indices [I>2σ(I)]	R$_{obs}$ = 0.0869, wR$_{obs}$ = 0.1622	R$_{obs}$ = 0.0323, wR$_{obs}$ = 0.0922	R$_{obs}$ = 0.0395, wR$_{obs}$ = 0.1063	R$_{obs}$ = 0.0901, wR$_{obs}$ = 0.2062
R indices [all data]	R$_{all}$ = 0.1471, wR$_{all}$ = 0.1686	R$_{all}$ = 0.0365, wR$_{all}$ = 0.0941	R$_{all}$ = 0.0612, wR$_{all}$ = 0.1296	R$_{all}$ = 0.1136, wR$_{all}$ = 0.2138
Largest diff. peak and hole	3.97 and -4.88 e·Å^{-3}	1.44 and -1.23 e·Å^{-3}	2.014 and -1.382 e·Å^{-3}	11.07 and -5.34 e·Å^{-3}
Compound	(4AMP)PbI$_4$	(4AMP) (MA)Pb$_2$I$_7$	(4AMP) (MA)$_2$Pb$_3$I$_{10}$	(4AMP) (MA)$_3$Pb$_4$I$_{13}$
Empirical formula	C$_6$N$_2$H$_{16}$PbI$_4$	(C$_6$N$_2$H$_{16}$)(CH$_3$NH$_3$)Pb$_2$I$_7$	(C$_6$N$_2$H$_{16}$)(CH$_3$NH$_3$)$_2$Pb$_3$I$_{10}$	(C$_6$N$_2$H$_{16}$)(CH$_3$NH$_3$)$_3$Pb$_4$I$_{13}$
Crystal system	Monoclinic			
Space group	*Pc*	*Ia*	*Pc*	*Ia*
Unit cell dimensions	a = 10.4999(13) Å, b = 12.5429(9) Å, c = 12.5289(13) Å, β = 89.984(9)°	a = 8.8412(11) Å, b = 8.8436(4) Å, c = 33.6045(5) Å, β = 90°	a = 23.1333(7) Å, b = 8.8365(3) Å, c = 8.8354(3) Å, β = 90°	a = 8.8587(18) Å, b = 8.8571(18) Å, c = 58.915(12) Å, β = 90°
Volume (Å^3)	1650.05(43)	2627.5(4)	1806.11(10)	4622.6(16)
Z	4	4	2	4
Density (g/cm^3)	3.3441	3.6681	3.8081	3.8666
Indepd. refl.	4646 [R$_{int}$ = 0.1198]	4558 [R$_{int}$ = 0.028]	7954 [R$_{int}$ = 0.0291]	8002 [R$_{int}$ = 0.1339]
Data / restraints / param.	4646 / 36 / 141	4558 / 17 / 116	7954 / 18 / 158	8002 / 19 / 202
Final R indices [I>2σ(I)]	R$_{obs}$ = 0.0797, wR$_{obs}$ = 0.1093	R$_{obs}$ = 0.0330, wR$_{obs}$ = 0.0915	R$_{obs}$ = 0.0351, wR$_{obs}$ = 0.0889	R$_{obs}$ = 0.0585, wR$_{obs}$ = 0.0839
R indices [all data]	R$_{all}$ = 0.1618, wR$_{all}$ = 0.1275	R$_{all}$ = 0.0410, wR$_{all}$ = 0.0949	R$_{all}$ = 0.0559, wR$_{all}$ = 0.0970	R$_{all}$ = 0.1700, wR$_{all}$ = 0.1000
Largest diff. peak and hole	4.48 and -4.31 e·Å^3	1.69 and -1.20 e·Å^{-3}	1.80 and -1.39 e·Å^{-3}	4.23 and -2.94 e·Å^{-3}

R = Σ||F$_o$|-|F$_c$|| / Σ|F$_o$|, wR = {Σ[w(|F$_o$|^2 - |F$_c$|^2)^2] / Σ[w(|F$_o$|^4)]}$^{1/2}$ and w=1/(σ^2(I)+0.0004I^2)
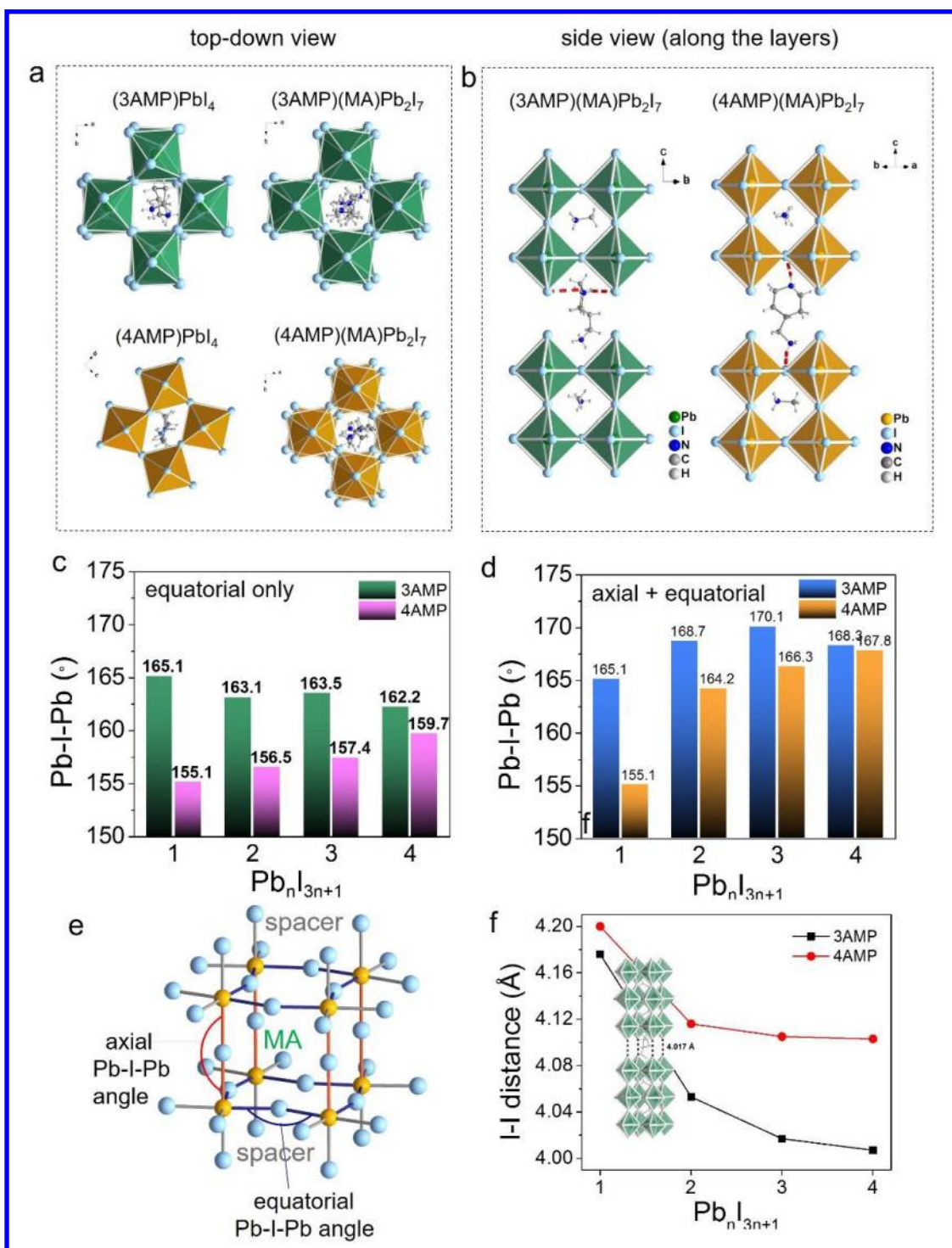
Figure 2. **a**, Top-view of (3AMP)PbI$_4$, (4AM)PPbI$_4$, (3AMP)(MA)Pb$_2$I$_7$ and (4AMP)(MA)Pb$_2$I$_7$. **b**, Side-view of (3AMP)(MA)Pb$_2$I$_7$ and (4AMP)(MA)Pb$_2$I$_7$, hydrogen bonding is marked in red. **c**, Average equatorial Pb-I-Pb angles for 3AMP and 4AMP series from n = 1 to 4. **d**, Average axial and equatorial angles for 3AMP and 4AMP. **e**, Definition of axial and equatorial Pb-I-Pb angles. **f**, I···I distance trend in 3AMP and 4AMP, where the 3AMP series has closer distance.

calculations are in good agreement with the observed trends. We further demonstrate the superior optoelectronic properties of these materials on photovoltaic (PV) devices. Owing to the less distorted crystal structure the 3AMP series shows a superior performance (~7% champion efficiency for n = 4) to the 4AMP series (~5% champion efficiency for n = 4). These two series of examples showcase the power of utilizing different templating organic cations to influence the semiconducting properties of the inorganic part of the perovskites, which broaden the horizons of 2D perovskites for achieving new solar cells and other optoelectronic devices with better characteristics.

Results and discussion

The structural differences between RP and DJ halide perovskites are mainly caused by the inter-layer cations (spacers), where RP phases have two sheets of interdigitating cations (1+) while the DJ phases only have one sheet of inter-layer cations (2+) between the inorganic slabs. The influence of the spacers on inorganic slabs is exerted in many levels, depending on the cation size and shape (steric effect), charge (electrostatic attraction) and the position of the functional groups (H-bonding and dispersion forces). This difference between RP and DJ perovskites is also reflected on the general formula, where RP phase has a general formula of $A'_2A_{n-1}M_nX_{3n+1}$ and DJ phase has a general formula of $A'A_{n-1}M_nX_{3n+1}$ (A' = inter-layer cation). In hybrid DJ phases, the inter-layer organic cations are 2+, having less degrees of freedom, making the layers closer to each other. In RP phases, the organic cations are 1+, which results in more flexible layer stacking.

The Dion-Jacobson series of layered perovskites, $(A')(MA)_{n-1}Pb_nI_{3n+1}$ (A' = 3AMP or 4AMP, n = 1- 4), produce uniform, square plate-like crystals, except 3-AMPPbI$_4$, which is an elongated plate as seen in Figure 1c. For the 3AMP series, the color of the crystal gets progressively darker from n = 1 (red) to n = 4 (black). The 4AMP has a similar trend, but it starts from lighter colors than the 3AMP for the n = 1 (orange) and n = 2 (red) members. The bulk crystals exhibit good stability in ambient environment and can be handled without any protection during characterizations.

Both $(A')(MA)_{n-1}Pb_nI_{3n+1}$ series form isostructural analogues for n>1. Detailed crystallographic data and structural refinements for all eight compounds reported here are listed in Table 1. They consist of n layers (~6.3 Å is the thickness of one octahedron) of corner-sharing $[PbI_6]^{4-}$ octahedra with xAMP^{2+} (x = 3, 4) separating the perovskite slabs and MA$^+$ filling in the perovskite voids (Figure 1b). The difference between the two DJ perovskite families is highlighted in Figure 2a and 2b, where specific crystallographic characteristics are stressed. The n = 1 and n = 2 members of each AMP series are selected as representative examples. For n = 1, the layers stack almost exactly on top of one another from the top-down viewing direction. (3AMP)PbI$_4$ is somewhat mismatched due to an out-of-plane tilting. (4AMP)PbI$_4$ matches perfectly as it displays exclusively large in-plane tilting. The 3AMP and 4AMP behave alike when it comes to n = 2, where the difference only lies in the Pb-I-Pb angle. The trend continues for the higher numbers (n = 3 and 4). Viewing along the inorganic layers (Figure 2b), the hydrogen bonding networks for 3AMP and 4AMP are drastically different. In (3AMP)(MA)Pb$_2$I$_7$, the 3AMP cation forms weak H-bonds (highlighted in red) with the terminal I$^-$. Bonding with the terminal I$^-$ has a small effect on the in-plane Pb-I-Pb angles as the terminal I$^-$ does not contribute to the in-plane distortion directly. On the contrary, in (4AMP)(MA)Pb$_2$I$_7$, the H-bonds are formed with the bridging I$^-$ anions deeper inside the layers as seen in Figure 2b, which amplify the in-plane distortion.

The differences in hydrogen bonding have an impact on the Pb-I-Pb angles, which are directly related to the optical and electrical these materials (see below). To illustrate this point, we classify the Pb-I-Pb angles into two categories, the axial (along the longest crystallographic axis) and the equatorial (along the inorganic plane) as shown in Figure 2e. In these systems, the axial Pb-I-Pb angles are very close to 180°, as they are much less affected by the interaction (e.g. hydrogen bonding) with the spacing cations. On the

other hand, the equatorial Pb-I-Pb angles are much more distorted since they are directly exposed to the spacing cations, especially for the case of n = 1 and n = 2. The evolution of the Pb-I-Pb angles is summarized in Figure 2c and 2d, where Figure 2c shows only the averaged equatorial angles and Figure 2d shows the averaged (both axial and equatorial) Pb-I-Pb angles. From Figure 2c, it is clear the gap between the average of the equatorial angles of the 3AMP and 4AMP gradually closes as the layer thickness increases from n = 1 to 4. For 3AMP, the averaged equatorial Pb-I-Pb decreases from 165.1° to 162.2° while for 4AMP it increases from 155.1° to 159.7°. This indicates that the effect of organic cation on the inorganic slabs is gradually diminished as they get thicker (increasing n number). As the axial Pb-I-Pb angles in both series are close to 180°, when they are averaged with the equatorial angles as shown in Figure 2d, the average is increased for both series up to n = 4.

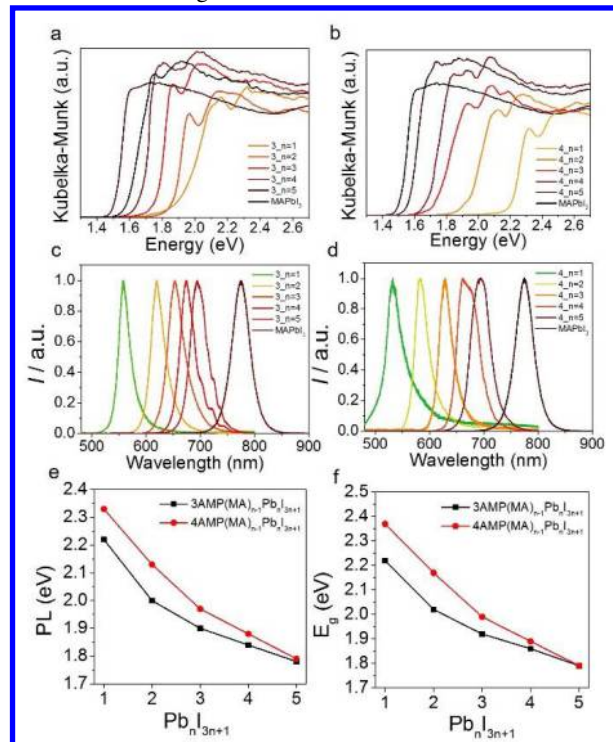Another interesting structural feature is that the I···I distance be-

Figure 3. Optical properties of the 3AMP and 4AMP series. **a,b**, Optical absorption spectra of 3AMP and 4AMP series. **c,d**, Steady-state photoluminescence (PL) spectra of 3AMP and 4AMP series. **e,f**, Summary of absorption and PL in energy from n = 1 to 5.
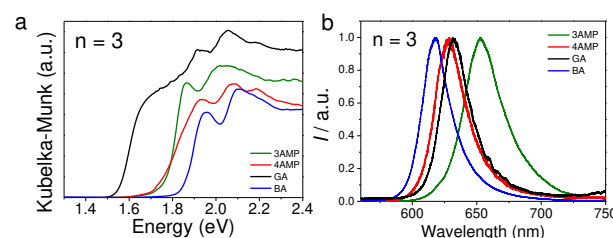
Figure 4. Comparison of the **a.** optical absorption spectra and **b.** PL spectra between (3AMP)(MA)$_2$Pb$_3$I$_{10}$, (4AMP)(MA)$_2$Pb$_3$I$_{10}$, (GA)(MA)$_3$Pb$_3$I$_{10}$ and (BA)$_2$(MA)$_2$Pb$_3$I$_{10}$.

tween the inorganic layers is very short. Since the layers lay exactly

Table 2. Optical properties and color of the (A')(MA)$_{n-1}$Pb$_n$I$_{3n+1}$ (A' = 3AMP or 4AMP, n = 1- 4) DJ perovskites.

	Compound	*E$_g$ (eV)*	*PL (eV)*	*Color*	*Compound*	*E$_g$ (eV)*	*PL (eV)*	*Color*
n = 1	(3AMP)PbI$_4$	2.23	2.22	red	(4AMP)PbI$_4$	2.38	2.33	orange
n = 2	(3AMP)(MA)Pb$_2$I$_7$	2.02	2.00	dark red	(4AMP)(MA)Pb$_2$I$_7$	2.17	2.13	red
n = 3	(3AMP)(MA)$_2$Pb$_3$I$_{10}$	1.92	1.90	black	(4AMP)(MA)$_2$Pb$_3$I$_{10}$	1.99	1.97	black
n = 4	(3AMP)(MA)$_3$Pb$_4$I$_{13}$	1.87	1.84	black	(4AMP)(MA)$_3$Pb$_4$I$_{13}$	1.89	1.88	black

on top of each other (eclipsed configuration), the I···I distance essentially defines the closest interlayer distance. The 3AMP series has generally smaller I···I distance than 4AMP (Figure 2d), while for both series the I···I distance gradually decreases slightly as the layer gets thicker. This is possibly a result of increased stacking fault formation in the perovskite layers as n increases, expressed indirectly in the determined average crystallographic structure. The close I···I interlayer distance (~ 4.0 Å) is one of the shortest among reported 2D lead iodide perovskites and plays a crucial role in affecting the electronic band structure of these materials which will be discussed below.

The optical band gaps of both 3AMP and 4AMP series follow a general trend that has the energy gap (E$_g$) decreasing as the layer number (n) increases (Table 2). From n = 1 to n = ∞ (MAPbI$_3$), the band gap decreases from 2.23 eV to 1.52 eV for the 3AMP series, while for the 4AMP the range is much wider (2.38 eV to 1.52 eV) (Figures 3a, 3b). The spectra of both series show clear excitonic features similarly to other 2D perovskites,[13, 18, 28, 51-52] which become less prominent as the n number increases and finally disappear for n = ∞. The steady-state photoluminescence (PL) spectra of these materials, shown in Figures 3c, d, exhibit an analogous trend with the band gaps. The 3AMP series demonstrates constantly lower PL emission energy than the 4AMP, until n = 5 when they become equal. Though the evolution of the band gap of both series matches the PL trend, from n = 3 and above, the difference between the two series is negligible (Figures 3e, f). The lifetimes of both AMP series (Figure S6) are comparable to the previously

reported 2D layered perovskite PEA (PEA = phenylethylamine) series, for which the lifetimes lie in the 0.1 – 0.2 ns range.[53] Overall the 3AMP series has longer lifetime than the 4AMP (except n = 1), which indicates slower carrier combination, more ideal for the PV devices.

The optical properties of the DJ iodide perovskites are quite different from those observed in RP perovskites.[51] Relative to the corresponding RP perovskites (Figure 4), the emission energy observed in PL is characteristically red shifted by ~ 0.1 eV in the case of 3AMP (1.90 eV) and 0.03 eV in the case of 4AMP (1.97 eV) with respect to the BA analogue (2.00 eV), taking n = 3 as the reference example.[51] The absorption edges of the compounds containing AMPs (1.70 eV) are also 0.1 eV lower than the BA analogue. The recently reported structural type ACI perovskite GAMA$_3$Pb$_3$I$_{10}$ falls in between the RP and DJ perovskites, with a E$_g$ of 1.73 eV and PL emission peak at 1.96 eV. [29]

The optical properties of these materials correlate very well with their structural characteristics. As discussed above, the Pb-I-Pb angles for 3AMP are systematically larger than the 4AMP. The larger Pb-I-Pb bond angles (closer to 180˚), the more the Pb s and I p orbitals overlap.[54-56] The strong anti-bonding interaction pushes up the valence band maximum (VBM), resulting in a reduced band gap. Thus, the systematically narrower band gap observed for 3AMP vs 4AMP can be attributed to the more linear Pb-I-Pb angles (i.e. smaller octahedral tilting (Figure S7))for the former.
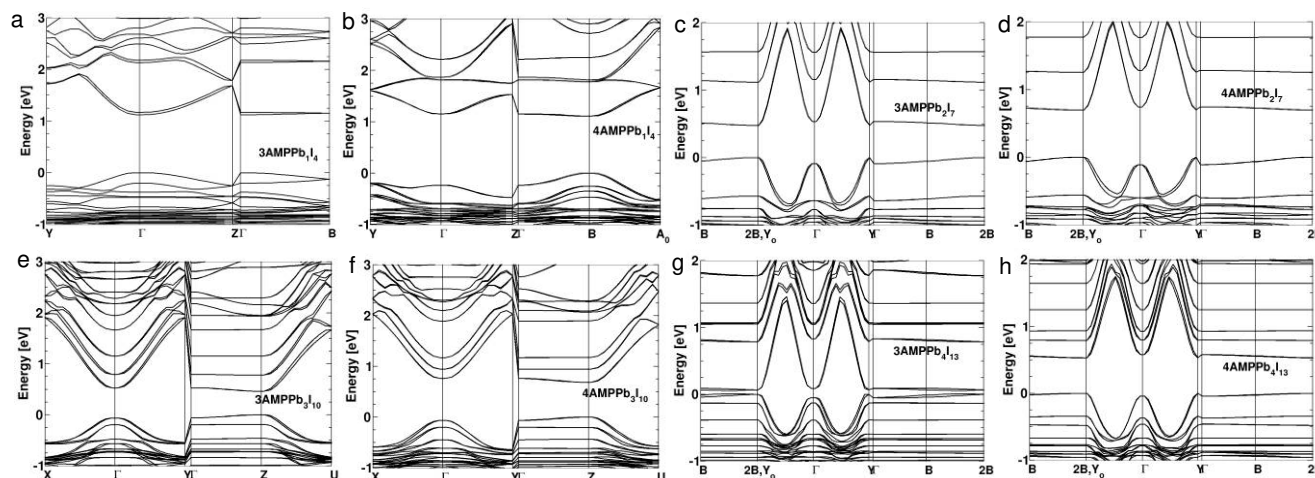

Figure 5. **a-g**, DFT calculations of band structures for the 3AMP and 4AMP series with SOC. The calculated gaps are 1.13 eV for (3AMP)PbI$_4$(*at Γ*), 1.14 eV for (4AMP)PbI$_4$ (*at B*), 0.48 eV for (3AMP)(MA)Pb$_2$I$_7$ *(at Y$_o$)*, 0.70 eV for (4AMP)(MA)Pb$_2$I$_7$ *(at Y$_o$)*, 0.47 eV for (3AMP)(MA)$_2$Pb$_3$I$_{10}$ *(at Z)*, 0.74 eV for (4AMP)(MA)$_2$Pb$_3$I$_{10}$ *(at Z)*, 0.07eV for (3AMP)(MA)$_3$Pb$_4$I$_{13}$ *(at Y$_o$)*, 0.54 eV for (4AMP)(MA)$_3$Pb$_4$I$_{13}$ *(at Y$_o$)*

The results of Density Functional Theory (DFT) electronic structure calculations are shown in Figure 5a-g. The calculated band gap for (3AMP)PbI$_4$ is determined at the Γ point (1.13 eV) (Figure 5a), whereas the band gap of (4AMP)PbI$_4$ is determined at the BZ edge (1.14 eV) (Figure 5b). The calculated band gaps for the higher numbers between the 3AMP and 4AMP series have larger differences, where E_g is 0.48 eV for n = 2, 3AMP, and 0.70 eV for n = 2, 4AMP (Figure 5c- d). For n = 3, the band gaps at Z point for 3AMP and 4AMP are 0.47 eV and 0.74 eV, respectively (Figure 5e -f). The calculated gap for 3AMP (n = 4) is very small (0.07 eV), much lower than 0.54 eV for n = 4, 4AMP as seen in Figure 5g -h. The DFT computed band gaps do not include many-body interactions needed to properly assess optical response, which is why calculated values are systematic underestimated without GW corrections.[57] The band gaps of 3AMP series DJ are systematically smaller than those computed for 4AMP series as shown in Figure 5h, in agreement with experimental findings. The stacking of perovskite sheets in the DJ structure type, which aligns the perovskite layers, allows for a better interlayer electronic coupling through van der Waals I···I interactions. These I···I contacts participate in anti-bonding interactions that further destabilize the VBM (Figure S9), contributing to the reduction of the band gap as compared to RP phases with respect to the same n-value, as discussed above.

Based on the attractive properties of the new 2D DJ perovskites, in a preliminary study we investigated the higher layer numbers (n = 3 and 4) as light absorbers for solar cells. A planar solar cell structure was adopted for device fabrication (Figure 6a), consisting of a fluorine doped tin oxide (FTO) substrate, a poly(3,4-ethylenedioxythiophene) polystyrene sulfonate (PEDOT:PSS) hole transport layer (HTL), a 2D perovskite light absorber, a C$_{60}$/BCP electron transport layer (ETL) and a Ag electrode. The devices were fabricated using a modified solvent engineering method (see Methods). The photocurrent density-voltage (J-V) curves of the solar cells using the 2D DJ perovskites are in Figure 6b, (measured using a reverse voltage scan). The thickness of the perovskite films was ~250 nm. Among the n = 3 and 4 for 3AMP and 4AMP, (3AMP)(MA)$_3$Pb$_4$I$_{13}$ achieved the highest power conversion efficiency (PCE) of 7.32% with a short-circuit current density (J$_{sc}$) of 10.17 mA·cm^{-2}, an open-circuit voltage (V$_{oc}$) of 1.06 V, and a fill factor (FF) of 67.60%. This value is significantly higher that the corresponding n = 3 and n = 4 RP perovskites prepared using a regular mesoporous TiO$_2$ device structure.

The remarkable performance of (3AMP)(MA)$_3$Pb$_4$I$_{13}$ can be mainly attributed to the reduced band gap and the improved mobility originating from the increased band dispersion (see above). While the device based on (3AMP)(MA)$_2$Pb$_3$I$_{10}$ has the lowest PCE of 2.02% with a J$_{sc}$ of 3.05 mA·cm^{-2}, a V$_{oc}$ of 0.99 V, and a FF of 66.54%, attributed to the largest band gap and the intense presence of a secondary phase, identified as the n = 2 member ($2\theta = ~11°$ and $~16°$). (4AMP)(MA)$_2$Pb$_3$I$_{10}$ and (4AMP)(MA)$_3$Pb$_4$I$_{13}$ have PCE below 5%, mainly due to the much lower J$_{sc}$ relative to the 3AMP. The average photovoltaic parameters of the devices using the various absorbers are summarized in Table S6. The J$_{sc}$ integrated from the external quantum efficiency (EQE) curves (Figure 6c) of the devices based for (3AMP)(MA)$_2$Pb$_3$I$_{10}$, (3AMP)(MA)$_3$Pb$_4$I$_{13}$, (4AMP)(MA)$_2$Pb$_3$I$_{10}$ and (4AMP)(MA)$_3$Pb$_4$I$_{13}$ are 2.92, 10.16, 5.83, and 7.08 mA·cm^{-2}, respectively, which are in good agreement with the trend of the J$_{sc}$ obtained from the J-V curves. In Figure 6d, powder x-ray diffraction (PXRD) of the (3AMP)(MA)$_3$Pb$_4$I$_{13}$, (4AMP)(MA)$_2$Pb$_3$I$_{10}$ and (4AMP)(MA)$_3$Pb$_4$I$_{13}$ films show preferred orientation in the "perpendicular" direction judging from the strongest *hkl* (110) and (220) at ~14° and ~28°, which facilitates the carriers to travel through

the layers.[8, 13] Further results of the fabrication of higher quality films and higher efficiency solar cells will be reported in the future. PL emission properties of the films (Figure 6e) are quite different (red shifted) from the bulk materials, which can be attributed to the so-called "edge effect".[52] The edge effect is observed in single crystals of both 3AMPPbI$_4$ and (3AMP)(MA)$_2$Pb$_3$I$_{10}$ as seen in Figure S11. The second PL emission at lower energy were observed when excited the sample through "the edge", which is parallel to the layers. The results show larger separation of the higher (2.21 eV from bulk) and lower energy emission (1.64 eV edge) of the n = 1 than for n = 3 (1.91 eV and 1.68 eV) for 3AMP. The lower energy emission (1.68 eV) is very close to the emission of the thin film (1.66 eV). This result is similar to the previously reported (BA)$_2$(MA)$_2$Pb$_3$I$_{10}$ example, where the higher energy emission is 2.00 eV and lower energy emission is 1.70 eV.[52] Attempts for measuring edge states of the other layered number crystals such as n = 2 and 4 were not successful owing to the thin crystal morphology which has caused handing difficulty.

The absorption edges of the films have the same trend as in the EQE spectra, though multiple slopes appear, indicating the for-
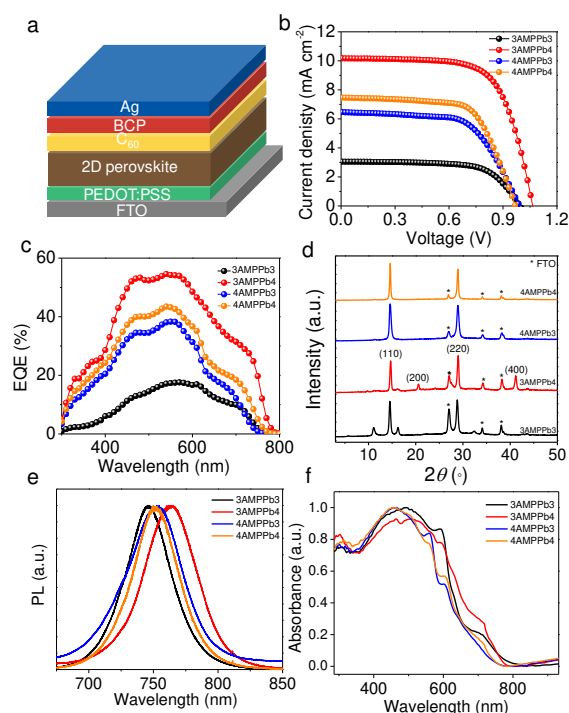

Figure 6. Solar cell architecture for the higher layer numbers (n = 3 and 4) of 3AMP and 4AMP. **a,** Scheme of the adopted inverted device structure. **b,** J-V curves of the 2D perovskite solar cell devices. **c,** External quantum efficiency (EQE) spectra. **d,** PXRD of the thin-films. **e,** steady-state PL spectra, where the emission peaks: 746 nm, 1.66 eV(3AMPPb$_3$I$_{10}$), 764 nm, 1.62 eV (3AMPPb$_4$I$_{13}$), 752 nm, 1.65 eV (4AMPPb$_3$I$_{10}$ and 4AMPPb$_4$I$_{13}$). **f,** Absorption spectra for the thin-films.

mation of some lower layer numbers (Figure 6f). Even though these 2D DJ perovskite devices are not completely optimized, the initial results show great promise as they compare well with the corresponding 2D RP perovskites which lead the 2D perovskite solar cells field.[8, 15, 58]

Conclusions

We have shown that a new crystal motif based on the DJ class of perovskites forms 2D hybrid lead iodide perovskites. The

special spacer cations used 3AMP and 4AMP have strong influence on the overall properties. Detailed crystallographic investigations on all eight compounds (n = 1 to 4, for 3AMP and 4AMP), have provided the structural insights for understanding the structure-property relationships. In particular, by understanding the angular distortion (Pb-I-Pb angle) within the system, we manage to show the subtle difference in the cations causes large differences in the optical properties by affecting the Pb-I-Pb angles, where the 3AMP series has systematically larger angles and smaller band gaps than the 4AMP series. Compared to the most common 2D RP perovskites, namely the BA series, the 3AMP and 4AMP series possess lower band gaps because of a less distorted inorganic framework and closer I···I interlayer distances. Our analysis suggests more superior optoelectronic properties of the 3AMP over the 4AMP series, which as demonstrated in the actual device fabrication, where the preliminary result shows the champion device has PCE over 7%. The strong correlation between the materials and their applications' performance validates the importance of understanding structure-property relationships and discovering new materials in the halide perovskite systems.

Methods

Materials. PbO (99.9%), 3-(aminomethyl)piperidine (Aldrich[CPR]), 4-(aminomethyl)piperidine (96%), hydroiodic acid (57 wt. % in H_2O, distilled, stabilized, 99.95%) and hypophosphorous acid solution (50 wt. % in H_2O) were purchased from Sigma-Aldrich and used as received. Methylammonium iodide (>99.5%) was purchased from Luminescence Technology Corp. and used as received.

Synthesis of $(3AMP)(MA)_{n-1}Pb_nI_{3n+1}$. For **n = 1**, an amount of 669 mg (3 mmol) 99.9% PbO powder was dissolved in 6 ml of hydroiodic acid and 1 ml hypophosphorous acid solution by heating under stirring for 5-10 min at ~130°C until the solution turned to clear bright yellow. 0.5 ml hydroiodic acid was added to 342 mg (3 mmol) 3-(aminomethyl)piperidine (3AMP) in a separate vial under stirring. The protonated 3AMP solution was added into the previous solution under heating and stirring for 5 min. Red plate-like crystals precipitate during slow cooling to room temperature. Yield 963 mg (38.6% based on total Pb content). For **n = 2**, an amount of 669 mg (3 mmol) 99.9% PbO powder was dissolved in 6 ml of hydroiodic acid and 1 ml hypophosphorous acid solution by heating under stirring for 5-10 min at 130°C until the solution turned to clear bright yellow. 318 mg (2 mmol) of methylammonium iodide (MAI) was added directly to the above solution under heating. 0.5 ml hydroiodic acid was added to 57 mg (0.5 mmol) 3AMP in a separate vial under stirring. The protonated 3AMP solution was added into the previous solution under heating and stirring for 5 min. Dark red plate-like crystals precipitated (Figure 1c) during slow cooling to room temperature. Yield 487 mg (22.4% based on total Pb content). For the synthesis of higher numbers, they follow the same route except the ratio were change to 37.6 mg (0.33 mmol) 3AMP, 477 mg (3 mmol) MAI, 669 mg (3 mmol) PbO for **n = 3,** yield 252 mg (12.2% based on total Pb content) and 34.2 mg (0.3 mmol) 3AMP, 636 mg (4 mmol) MAI, 892 mg (4 mmol) PbO for **n = 4**, yield 301 mg (11.2% based on total Pb content).

Synthesis of $(4AMP)(MA)_{n-1}Pb_nI_{3n+1}$. Similar synthetic procedures were used to synthesize the 4AMP series. However, the amount of 4AMP was reduced as the 4AMP series precipitate faster than the 3AMP. The experimental ratios (4AMP: MAI: PbO) (in mmol) of the 4AMP are 3:0:3 for n = 1, 0.5:2:3 for n = 2, 0.33:3:3 for n = 3 and 0.27:4:4 for n = 4. Yield 1155 mg (46.3%), 684 mg

(31.5%), 531 mg (25.6%) and 477 mg (17.7% based on total Pb content), respectively.

Powder X-ray Diffraction. PXRD analysis was performed using a Rigaku Miniflex600 powder X-ray diffractometer (Cu Kα graphite, λ = 1.5406 Å) operating at 40 kV/15 mA with a Kβ foil filter.

Single Crystal X-ray Diffraction. Full sphere data were collected after screening for a few frames using either a STOE IPDS 2 or IPDS 2T diffractometer with graphite-monochromatized Mo Kα radiation (λ = 0.71073 Å) (50 kV/40 mA) under N_2 at 293 K ($3AMPPbI_4$, $4AMPPbI_4$ and $(3AMP)(MA)_3Pb_4I_{13}$). The collected data was integrated and applied with numerical absorption corrections using the STOE X-AREA programs. The rest of the compounds were collected using a Bruker Molly instrument with MoKα IμS microfocus source (λ = 0.71073 Å) with MX Optics at 250 K. The collected data was integrated and applied with numerical absorption corrections using the APEX3 software. Crystal structures were solved by charge flipping and refined by full-matrix least squares on F^2 with the Jana2006 package.

Optical Absorption Spectroscopy. Optical diffuse reflectance measurements were performed using a Shimadzu UV-3600 UV-VIS-NIR spectrometer operating in the 200 – 1000 nm region using $BaSO_4$ as the reference of 100% reflectance. The band gap of the material was estimated by converting reflectance to absorption according to the Kubelka–Munk equation: $\alpha/S = (1–R)^2(2R)^{-1}$, where R is the reflectance and α and S are the absorption and scattering coefficients, respectively.

Steady State and Time-resolved Photoluminescence. Steady-state PL spectra were collected using HORIBA LabRAM HR Evolution Confocal RAMAN microscope. 473 nm laser (0.1% power) was used to excite all samples at 50× magnification. Time-resolved photoluminescence (TRPL) spectra were acquired using HORIBA Fluorolog-3 equipped with a 450-W xenon lamp and a TCSPC module (diode laser excitation at λ = 375 nm) and an integrating sphere (Horiba Quanta–φ) for absolute photoluminescence quantum yield determination. The spectra were corrected for the monochromator wavelength dependence and photomultiplier response functions provided by the manufacturer.

Electronic Structure Calculations. First-principles calculations are based on density functional theory (DFT) as implemented in the VASP package.[59-61] All calculations are carried out on the experimentally determined crystal structures. We used the GGA functional in the PBE form, the projector augmented wave (PAW) method[62-63] with the PAW data set supplied in the VASP package with the following valence orbitals: Pb [$5d^{10}6s^26p^2$], I [$5s^25p^5$], N [$2s^22p^3$], H [$1s^1$] and C [$2s^22p^2$]. In addition, the wavefunctions are expanded using a plane-wave basis set with an energy cut-off of 500 eV. Spin-orbit coupling is systematically taken into account. For band structures, the reciprocal space integration is performed over a 4×4×1 Monkhorst-Pack grid for compounds with n=1 and n=3, and over a 4x4x4 grid for compounds with n=2 and n=4 in their primitive cells.[64-65]

Device fabrications. FTO glass substrates were coated with PEDOT:PSS by spin-coating at 4000 rpm for 30s, and then annealed at 150 °C for 30 min in air. The 2D perovskite precursors with a molar concentration of 0.6 M were prepared by dissolving the 2D perovskite crystal powders in a mixed solvent of DMF and DMSO with a volume ratio of 4:1. After the crystal powders dissolved, adding 0.8 vol% HI into the perovskite precursors. Then the precursors were coated on the substrates with a spin rate of 4000 rpm for 60s in a N2-filled glove box. During the spin-coating, 0.7 mL diethyl ether was dropped on the rotating substrates at 20 s.

After spin-coating, the films were annealed at 100 °C for 10 min in the glove box. To complete the devices, C60 (20 nm)/BCP (5 nm)/Ag (100 nm) were sequentially thermally evaporated on top of the perovskites. The active area of the solar cells was 0.09 cm^2.

Characterizations. J-V curves were measured by a Keithley model 2400 instrument under AM1.5G simulated irradiation with a standard solar simulator (Abet Technologies). The light intensity of the solar simulator was calibrated by a National Renewable Energy Laboratory-certified monocrystalline silicon solar cell. EQE curves were measured by an Oriel model QE-PV-SI instrument equipped with a National Institute of Standards and Technology-certified Si diode.

ASSOCIATED CONTENT

Supporting Information

Additional crystallographic details (CIF), thermal analysis (DSC, TGA and DTA), calculation and device data (PDF). This material is available free of charge via the Internet at http://pubs.acs.org.

AUTHOR INFORMATION

Corresponding Author

*Email: m-kanatzidis@northwestern.edu

*konstantinos.stoumpos@northwestern.edu

ACKNOWLEDGMENT

REFERENCES

1. Kojima, A.; Teshima, K.; Shirai, Y.; Miyasaka, T., *J. Am. Chem. Soc.* **2009,** *131*, 6050-6051.
2. Yang, W. S.; Park, B.-W.; Jung, E. H.; Jeon, N. J.; Kim, Y. C.; Lee, D. U.; Shin, S. S.; Seo, J.; Kim, E. K.; Noh, J. H.; Seok, S. I., *Science* **2017,** *356*, 1376-1379.
3. Jeon, N. J.; Noh, J. H.; Kim, Y. C.; Yang, W. S.; Ryu, S.; Seok, S. I., *Nat. Mater.* **2014,** *13*, 897-903.
4. Mei, A.; Li, X.; Liu, L.; Ku, Z.; Liu, T.; Rong, Y.; Xu, M.; Hu, M.; Chen, J.; Yang, Y.; Grätzel, M.; Han, H., *Science* **2014,** *345*, 295-298.
5. Lee, M. M.; Teuscher, J.; Miyasaka, T.; Murakami, T. N.; Snaith, H. J., *Science* **2012,** *338*, 643-647.
6. Green, M. A.; Ho-Baillie, A.; Snaith, H. J., *Nat. Photon.* **2014,** *8*, 506-514.
7. Li, X.; Ibrahim Dar, M.; Yi, C.; Luo, J.; Tschumi, M.; Zakeeruddin, S. M.; Nazeeruddin, M. K.; Han, H.; Grätzel, M., *Nat. Chem.* **2015,** *7*, 703-711.
8. Tsai, H.; Nie, W.; Blancon, J.-C.; Stoumpos, C. C.; Asadpour, R.; Harutyunyan, B.; Neukirch, A. J.; Verduzco, R.; Crochet, J. J.; Tretiak, S.; Pedesseau, L.; Even, J.; Alam, M. A.; Gupta, G.; Lou, J.; Ajayan, P. M.; Bedzyk, M. J.; Kanatzidis, M. G.; Mohite, A. D., *Nature* **2016,** *536*, 312-316.
9. Yuan, M.; Quan, L. N.; Comin, R.; Walters, G.; Sabatini, R.; Voznyy, O.; Hoogland, S.; Zhao, Y.; Beauregard, E. M.; Kanjanaboos, P.; Lu, Z.; Kim, D. H.; Sargent, E. H., *Nat. Nanotechnol.* **2016,** *11*, 872-877.
10. Saparov, B.; Mitzi, D. B., *Chem. Rev.* **2016,** *116*, 4558-4596.
11. Stoumpos, C. C.; Kanatzidis, M. G., *Acc. Chem. Res.* **2015,** *48*, 2791-802.
12. Pedesseau, L.; Sapori, D.; Traore, B.; Robles, R.; Fang, H.-H.; Loi, M. A.; Tsai, H.; Nie, W.; Blancon, J.-C.; Neukirch, A.; Tretiak, S.; Mohite, A. D.; Katan, C.; Even, J.; Kepenekian, M., *ACS Nano* **2016,** *10*, 9776-9786.
13. Cao, D. H.; Stoumpos, C. C.; Farha, O. K.; Hupp, J. T.; Kanatzidis, M. G., *J. Am. Chem. Soc.* **2015,** *137*, 7843-50.
14. Smith, I. C.; Hoke, E. T.; Solis-Ibarra, D.; McGehee, M. D.; Karunadasa, H. I., *Angew. Chem. Int. Ed.* **2014,** *53*, 11232-11235.
15. Quan, L. N.; Yuan, M.; Comin, R.; Voznyy, O.; Beauregard, E. M.; Hoogland, S.; Buin, A.; Kirmani, A. R.; Zhao, K.; Amassian, A.; Kim, D. H.; Sargent, E. H., *J. Am. Chem. Soc.* **2016,** *138*, 2649–2655.
16. Liao, Y.; Liu, H.; Zhou, W.; Yang, D.; Shang, Y.; Shi, Z.; Li, B.; Jiang, X.; Zhang, L.; Quan, L. N.; Quintero-Bermudez, R.; Sutherland, B. R.; Mi, Q.; Sargent, E. H.; Ning, Z., *J. Am. Chem. Soc.* **2017,** *139*, 6693-6699.
17. Mao, L.; Tsai, H.; Nie, W.; Ma, L.; Im, J.; Stoumpos, C. C.; Malliakas, C. D.; Hao, F.; Wasielewski, M. R.; Mohite, A. D.; Kanatzidis, M. G., *Chem. Mater.* **2016,** *28*, 7781-7792.
18. Dohner, E. R.; Jaffe, A.; Bradshaw, L. R.; Karunadasa, H. I., *J. Am. Chem. Soc.* **2014,** *136*, 13154-13157.
19. Mao, L.; Wu, Y.; Stoumpos, C. C.; Wasielewski, M. R.; Kanatzidis, M. G., *J. Am. Chem. Soc.* **2017,** *139*, 5210–5215.
20. Congreve, D. N.; Weidman, M. C.; Seitz, M.; Paritmongkol, W.; Dahod, N. S.; Tisdale, W. A., *ACS Photonics* **2017,** *4*, 476-481.
21. Lanzetta, L.; Marin-Beloqui, J. M.; Sanchez-Molina, I.; Ding, D.; Haque, S. A., *ACS Energy Lett.* **2017,** *2*, 1662-1668.
22. Tsai, H.; Nie, W.; Blancon, J. C.; Stoumpos, C. C.; Soe, C. M. M.; Yoo, J.; Crochet, J.; Tretiak, S.; Even, J.; Sadhanala, A., *Adv. Mater.* **2018,** *30*, 1704217.
23. Stoumpos, C. C.; Mao, L.; Malliakas, C. D.; Kanatzidis, M. G., *Inorg. Chem.* **2017,** *56*, 56-73.
24. Du, K.-z.; Tu, Q.; Zhang, X.; Han, Q.; Liu, J.; Zauscher, S.; Mitzi, D. B., *Inorg. Chem.* **2017,** *56*, 9291-9302.
25. Hautzinger, M. P.; Dai, J.; Ji, Y.; Fu, Y.; Chen, J.; Guzei, I. A.; Wright, J. C.; Li, Y.; Jin, S., *Inorg. Chem.* **2017,** *56*, 14991-14998.
26. Calabrese, J.; Jones, N. L.; Harlow, R. L.; Herron, N.; Thorn, D. L.; Wang, Y., *J. Am. Chem. Soc.* **1991,** *113*, 2328-2330.
27. Stoumpos, C. C.; Cao, D. H.; Clark, D. J.; Young, J.; Rondinelli, J. M.; Jang, J. I.; Hupp, J. T.; Kanatzidis, M. G., *Chem. Mater.* **2016,** *28*, 2852-2867.
28. Stoumpos, C. C.; Soe, C. M. M.; Tsai, H.; Nie, W.; Blancon, J.-C.; Cao, D. H.; Liu, F.; Traoré, B.; Katan, C.; Even, J.; Mohite, A. D.; Kanatzidis, M. G., *Chem* **2017,** *2*, 427-440.
29. Soe, C. M. M.; Stoumpos, C. C.; Kepenekian, M.; Traoré, B.; Tsai, H.; Nie, W.; Wang, B.; Katan, C.; Seshadri, R.; Mohite, A. D.; Even, J.; Marks, T. J.; Kanatzidis, M. G., *J. Am. Chem. Soc.* **2017,** *139*, 16297-16309.
30. Mitzi, D. B.; Feild, C. A.; Harrison, W. T. A.; Guloy, A. M., *Nature* **1994,** *369*, 467-469.

31. Papavassiliou, G. C.; Mousdis, G. A.; Raptopoulou, C.; Terzis, A., *Z. Naturforsch. B Chem. Sci.* **2000,** *55*, 536-540.

32. Mercier, N., *CrystEngComm* **2005,** *7*, 429-432.

33. Zhu, X.-H.; Mercier, N.; Riou, A.; Blanchard, P.; Frère, P., *Chem. Commun.* **2002**, 2160-2161.

34. Mao, L.; Wu, Y.; Stoumpos, C. C.; Traore, B.; Katan, C.; Even, J.; Wasielewski, M. R.; Kanatzidis, M. G., *J. Am. Chem. Soc.* **2017,** *139*, 11956-11963.

35. Luo, J.; Li, L.; Sun, Z.; Wang, P.; Hu, W.; Wang, S.; Ji, C.; Hong, M., *Angew. Chem. Int. Ed.* **2017,** *129*, 12318–12322.

36. Nazarenko, O.; Kotyrba, M. R.; Wörle, M.; Cuervo-Reyes, E.; Yakunin, S.; Kovalenko, M. V., *Inorg. Chem.* **2017,** *56*, 11552-11564.

37. Schaak, R. E.; Mallouk, T. E., *Chem. Mater.* **2002,** *14*, 1455-1471.

38. Battle, P. D.; Green, M. A.; Lago, J.; Millburn, J. E.; Rosseinsky, M. J.; Vente, J. F., *Chem. Mater.* **1998,** *10*, 658-664.

39. Dion, M.; Ganne, M.; Tournoux, M., *Mater. Res. Bull.* **1981,** *16*, 1429-1435.

40. Hojamberdiev, M.; Bekheet, M. F.; Zahedi, E.; Wagata, H.; Kamei, Y.; Yubuta, K.; Gurlo, A.; Matsushita, N.; Domen, K.; Teshima, K., *Cryst. Growth Des.* **2016,** *16*, 2302-2308.

41. Kendall, K. R.; Navas, C.; Thomas, J. K.; zur Loye, H.-C., *Chem. Mater.* **1996,** *8*, 642-649.

42. Mousdis, G. A.; Papavassiliou, G. C.; Raptopoulou, C.; Terzis, A., *J. Mater. Chem.* **2000,** *10*, 515-518.

43. Rayner, M. K.; Billing, D. G., *Acta Cryst. E* **2010,** *66*, m660-m660.

44. Tang, Z.; Guan, J.; Guloy, A. M., *J. Mater. Chem.* **2001,** *11*, 479-482.

45. Lemmerer, A.; Billing, D. G., *CrystEngComm.* **2012,** *14*, 1954-1966.

46. Bulou, A.; Nouet, J., *J. Phys. C Solid State Phys.* **1982,** *15*, 183.

47. Tilley, R. J., *Perovskites: Structure-Property Relationships*. John Wiley & Sons: 2016; p 123-155.

48. Jacobson, A. J.; Lewandowski, J. T.; Johnson, J. W., *Mater. Res. Bull.* **1990,** *25*, 679-686.

49. Gopalakrishnan, J.; Bhat, V., *Inorg. Chem.* **1987,** *26*, 4299-4301.

50. Jacobson, A. J.; Johnson, J. W.; Lewandowski, J. T., *Inorg. Chem.* **1985,** *24*, 3727-3729.

51. Stoumpos, C. C.; Cao, D. H.; Clark, D. J.; Young, J.; Rondinelli, J. M.; Jang, J. I.; Hupp, J. T.; Kanatzidis, M. G., *Chem. Mater.* **2016,** *28*, 2852-2867.

52. Blancon, J.-C.; Tsai, H.; Nie, W.; Stoumpos, C. C.; Pedesseau, L.; Katan, C.; Kepenekian, M.; Soe, C. M. M.; Appavoo, K.; Sfeir, M. Y.; Tretiak, S.; Ajayan, P. M.; Kanatzidis, M. G.; Even, J.; Crochet, J. J.; Mohite, A. D., *Science* **2017,** *355*, 1288-1292.

53. Peng, W.; Yin, J.; Ho, K.-T.; Ouellette, O.; De Bastiani, M.; Murali, B.; El Tall, O.; Shen, C.; Miao, X.; Pan, J., *Nano lett.* **2017,** *17*, 4759-4767.

54. Knutson, J. L.; Martin, J. D.; Mitzi, D. B., *Inorg. Chem.* **2005,** *44*, 4699-4705.

55. Katan, C.; Pedesseau, L.; Kepenekian, M.; Rolland, A.; Even, J., *J. Mater. Chem. A* **2015,** *3*, 9232-9240.

56. Liu, G.; Kong, L.; Guo, P.; Stoumpos, C. C.; Hu, Q.; Liu, Z.; Cai, Z.; Gosztola, D. J.; Mao, H.-k.; Kanatzidis, M. G.; Schaller, R. D., *ACS Energy Lett.* **2017**, 2518-2524.

57. Even, J.; Pedesseau, L.; Dupertuis, M.-A.; Jancu, J.-M.; Katan, C., *Phys. Rev. B* **2012,** *86*, 205301.

58. Zhou, N.; Shen, Y.; Li, L.; Tan, S.; Liu, N.; Zheng, G.; Chen, Q.; Zhou, H., *J. Am. Chem. Soc.* **2017,** *140*, 459-465.

59. Kresse, G.; Furthmüller, J., *Phys. Rev. B* **1996,** *54*, 11169.

60. Kresse, G.; Furthmüller, J., *Comput. Mater. Sci.* **1996,** *6*, 15-50.

61. Shishkin, M.; Kresse, G., *Phys. Rev. B* **2006,** *74*, 035101.

62. Blöchl, P. E., *Phys. Rev. B* **1994,** *50*, 17953.

63. Kresse, G.; Joubert, D., *Phys. Rev. B* **1999,** *59*, 1758.

64. Monkhorst, H. J.; Pack, J. D., *Phys. Rev. B* **1976,** *13*, 5188.

65. Pack, J. D.; Monkhorst, H. J., *Phys. Rev. B* **1977,** *16*, 1748.

TOC Graphic

(A')(MA)$_{n-1}$Pb$_n$I$_{3n+1}$　(A' = 3AMP or 4AMP)

Dion-Jacobson phase

n = 1
n = 2
n = 3
n = 4

Pb
I
N
C
H